

# Relative Orbit Determination of Multiple Satellites Using Double Differenced Measurements

Jeroen L. Geeraert

Colorado Center for Astrodynamics Research, University of Colorado, Boulder, CO 80309.

Jay W. McMahon

Colorado Center for Astrodynamics Research, University of Colorado, Boulder, CO 80309.

## Abstract

The location of operational space assets around the Earth is still of primary concern in the SSA community due to the ever increasing density of man-made objects and potential for collisions. In this paper we demonstrate using the double differenced measurements of time difference of arrival (TDOA) and frequency difference of arrival (FDOA) for relative orbit determination of multiple satellites. A close proximity two-spacecraft formation with bounded orbits is presented to demonstrate the TDOA and FDOA OD capabilities. Two scenarios are examined, the first is with the chief satellite assumed to have perfectly known state knowledge, and the second assumes some small uncertainty on the chief satellite. In the first scenario a square-root unscented Kalman filter is used to estimate the state of the deputy about the chief, and in the second scenario the deputy satellite is estimated while the uncertainty of the chief satellite is considered using the square-root unscented Schmidt-Kalman filter. The OD results are compared with conventional range and range-rate measurements and we find that, with three baselines or more, the TDOA and FDOA provides the lowest uncertainty OD solutions except for the case where the chief is in a GEO orbit. When only one baseline is used, the TDOA and FDOA measurements are favorable with lower orbits and a longer observation spans.

## 1 Introduction

Using double differenced measurements of time difference of arrival (TDOA) and frequency difference of arrival (FDOA) can be an effective way to improve the relative orbit determination of a satellite formation. Precise tracking of spacecraft and operational assets is necessary in order to correctly assess whether collision avoidance maneuvers should or should not be implemented in densely populated volumes. While the TDOA and FDOA observables have not been significantly used for OD purposes before, they have close ties to the  $\Delta$ DOR and same-beam interferometry measurement types used for deep-space navigation which provide extremely accurate tracking.

In this paper we use both a square-root unscented Kalman filter (SR-UKF) and a square-root unscented Schmidt-Kalman filter (SR-USKF), also known as a square-root consider unscented Kalman filter see Ref. [2] for details. We first introduce the TDOA and FDOA measurement models as well as the range and range-rate measurement models to establish a point of comparison. Then we introduce the dynamics model and finally show an example of OD with a chief-deputy bounded relative motion case.

## 2 Measurement Models

### 2.1 TDOA and FDOA

Figure 1 illustrates the setup to generate the TDOA and FDOA measurements. The receiver (RX) dishes marked by  $RX_1$  and  $RX_2$  each represent a single receiver channel rather than the actual physical number of RXs required. Therefore in the current setup, while two RXs could be used, a single RX with two channels would likely be preferred. The two RXs and the reference transmitter (TX) are generally located in the same complex with  $i$  number of arbitrary TXs located across the continent which creates  $i$  baselines with the reference.

A waveform is generated by both the  $i^{th}$  TX and the reference TX (not necessarily the same waveform) which is intercepted by both the primary and secondary satellites. A bent pipe architecture on the satellites immediately returns

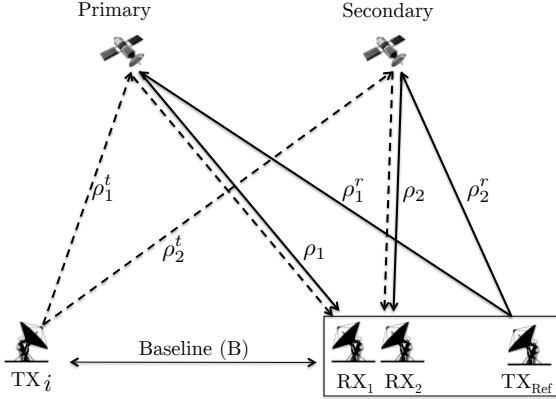


Figure 1: TDOA/FDOA Geometry

the signals back to Earth which are then acquired by the RXs. Temporarily ignoring the reference TX we see that the waveform generated by the  $i^{th}$  TX is received by both  $RX_1$  and  $RX_2$ , despite being the same waveform when emitted, the difference in path lengths to each of the satellites and the difference in relative motion causes a time delay and Doppler shift between the two received signals. Generally the time delay and Doppler shift are estimated jointly in order to determine either one adequately, this is done through a generalized form of the correlation process known as the complex ambiguity function (CAF) [5],

$$A(\tau, f) = \int_0^T [s_1(t)s_2^*(t + \tau)]^{-j2\pi ft} dt. \quad (1)$$

Where,  $s_1(t)$  and  $s_2(t)$  are the two waveforms to be correlated, and where  $*$  represents the complex conjugate. The time delay and frequency offsets are  $\tau$  and  $f$  respectively. The values of  $\tau$  and  $f$  that maximize  $|A(\tau, f)|$  are known as the differential time offset (DTO) and the differential frequency offset (DFO) respectively. Since the reference TX was previously ignored these DTO and DFO values correspond to the  $i^{th}$  TX denoted by the superscript  $t$  such that we have a  $DTO^t$  and  $DFO^t$ . Similarly we can correlate the waveforms from the reference TX to obtain  $DTO^r$  and  $DFO^r$  where the superscript  $r$  indicates the values associated with the reference TX. Finally the difference of the DTOs between the  $i^{th}$  and reference TX is TDOA,

$$TDOA = DTO^t - DTO^r. \quad (2)$$

While the difference of the DFOs between the  $i^{th}$  and reference TX is FDOA,

$$FDOA = DFO^t - DFO^r. \quad (3)$$

Naturally, the time delays and Doppler shifts are due to differing ranges and range-rates between the TXs, satellites and RXs. We can further derive TDOA and FDOA in terms of these variables, and thereby show that one of the major strengths of these observables is the cancellation of many common errors. We start by defining the pseudo-range as  $\tilde{\rho}$  shown in Eq. 4,

$$\tilde{\rho} = \rho + c\delta_{RX} + c\delta_{TX} + \delta_{\rho_{atm}} + \varepsilon. \quad (4)$$

Where  $\rho$  is the true range,  $c$  is the speed of light,  $\delta_{RX}$  is the receiver delay due to clock bias,  $\delta_{TX}$  is the transmitter delay also due to clock bias,  $\delta_{\rho_{atm}}$  are the path delays caused by the tropo and ionosphere, and finally  $\varepsilon$  are any other unaccounted for measurement errors. In a similar fashion the pseudo-range-rate  $\dot{\tilde{\rho}}$  is defined as the time derivative of pseudo-range,

$$\dot{\tilde{\rho}} = \dot{\rho} + c\dot{\delta}_{RX} + c\dot{\delta}_{TX} + \dot{\delta}_{\rho_{atm}} + \zeta. \quad (5)$$

Where,  $\dot{\rho}$  is the true range-rate,  $\dot{\delta}_{RX}$  is the receiver clock drift rate,  $\dot{\delta}_{TX}$  is the transmitter clock drift rate,  $\dot{\delta}_{\rho_{atm}}$  is the tropo and ionospheric delay rate, and finally  $\zeta$  are the additional unaccounted for measurement errors. Note that in Eqs. 4 and 5 these are one-way range and range-rates, therefore a TX can mean the actual ground-based TX but also

the satellite. Similarly a RX can mean the ground-based receiver but also the satellite depending on whether the range or range-rate is an uplink or a downlink signal.

Going through the motions of computing TDOA we obtain the following expression,

$$TDOA = \frac{1}{c} [\rho_2^t - \rho_2^r + \rho_1^r - \rho_1^t] + (\delta_{\rho_{atm_1}}^r - \delta_{\rho_{atm_2}}^r - \delta_{\rho_{atm_1}}^t + \delta_{\rho_{atm_2}}^t) + (\epsilon_1^r - \epsilon_2^r - \epsilon_1^t + \epsilon_2^t) \quad (6)$$

The subscripts 1 and 2 refer to the primary and secondary satellite. Using Figure 1 as a guide, notice how only the uplink components remain. Furthermore, all the clock biases of the TXs and RXs and therefore also the satellite translation oscillators have completely cancelled. Equation 6 shows that we are left with atmospheric delays as well as unaccounted for range errors. Examining the atmospheric errors we see that they effectively cancel to zero because the signal path to satellite 1 and 2 is nearly identical over the first 10's of kilometers of the signal path. In effect we can say that  $\delta_{\rho_{atm_1}}^r \approx \delta_{\rho_{atm_2}}^r$  and  $\delta_{\rho_{atm_1}}^t \approx \delta_{\rho_{atm_2}}^t$  as the localized atmospheric effects over each of the TXs are the same. Finally while the unaccounted for range errors are not completely cancelled, they are significantly reduced in magnitude due to the differencing between the  $i^{th}$  TX and reference TX. As a result the final TDOA equation is reduced to,

$$TDOA = \frac{1}{c} [\rho_2^t - \rho_2^r + \rho_1^r - \rho_1^t]. \quad (7)$$

Similarly for FDOA if the frequencies of the  $i^{th}$  TX  $f_{tr}^t$ , and the reference TX  $f_{tr}^r$ , are identical or at least approximately equal the same reduction approximation can be applied to yield,

$$FDOA = \frac{1}{c} [f_{tr}^t (\dot{\rho}_1^t + \dot{\rho}_1 - \dot{\rho}_2^t - \dot{\rho}_2) - f_{tr}^r (\dot{\rho}_1^r + \dot{\rho}_1 - \dot{\rho}_2^r - \dot{\rho}_2)]. \quad (8)$$

A key driver for the TDOA/FDOA system to work is that both satellites are required to be within the beamwidth or an accompanying side lobe of the transmitting antenna, inevitably restricting the angular separation of the two satellites [3]. Smaller antennas are consequentially preferred as they have wider beamwidths and provide a stronger signal to the secondary satellite which in turn improves the correlation of the DTO and DFO estimation [1].

Table 1 lists the simulated location of the reference TX as well as the two RXs and the three conjugate TXs that make up the baseline with the reference.

Table 1: Latitude, longitude and altitude of transmitters and receivers

<i>Transmitters (TXs)</i>			
<i>Reference Station</i>			
Boulder	40.015° N	105.270° W	1623.72 m
<i>Stations</i>			
San Diego	32.72° N	117.16° W	27.91 m
Seattle	47.60° N	122.33° W	9.44 m
Houston	29.76° N	95.37° W	14.54 m
<i>Receivers (RXs)</i>			
Boulder 1	40.014° N	105.271° W	1625.57 m
Boulder 2	40.014° N	105.270° W	1621.13 m

## 2.2 Range and Range-Rate

Due to the novelty of using TDOA and FDOA for orbit determination we opt to compare the results to the more commonly known tracking data of range and range-rate. Figure 2 aims to display a radar system which closely resembles the TDOA/FDOA setup from Figure 1. In the range and range-rate setup each dish represents a transceiver (T/RX) rather than just a TX or just a RX, each dish is also a channel rather than a physical antenna. The two T/RXs

on the right side of Figure 2 are in the same location as the reference TX and RXs from the TDOA/FDOA setup and are always taking measurements when both satellites are visible. The T/RXs on the left side are the  $i$  number of arbitrary T/RXs located across the continent in the same locations as those  $i$  TXs from the TDOA/FDOA system so as to replicate the same baselines.

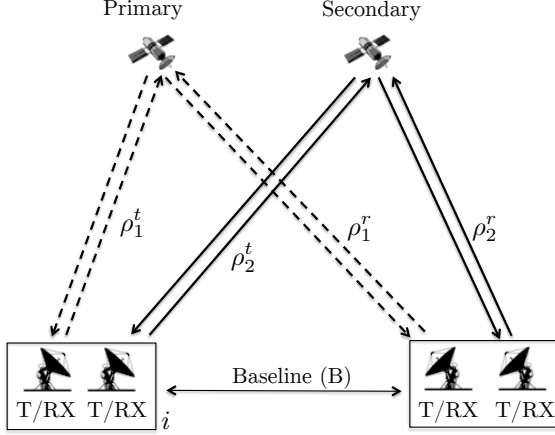


Figure 2: Range/Range-Rate Geometry

While with the TDOA/FDOA system there is one TDOA and one FDOA measurement per baseline per measurement time, the range/range-rate system provides four range and four range-rate measurements. This is four times as many measurements but maintains a comparable measurement geometry between the two systems. Note that the ranges and range-rates are defined by Eqs. 4 and 5. In this case however, none of the clock biases or drifts cancel and the full atmospheric and unaccounted for measurements errors are in effect.

### 3 Satellite State Dynamics

We consider the simplest case of 2-body motion without any perturbing forces acting upon the two satellites. A chief and a deputy satellite are defined such that the deputy is estimated relative to the chief satellite.

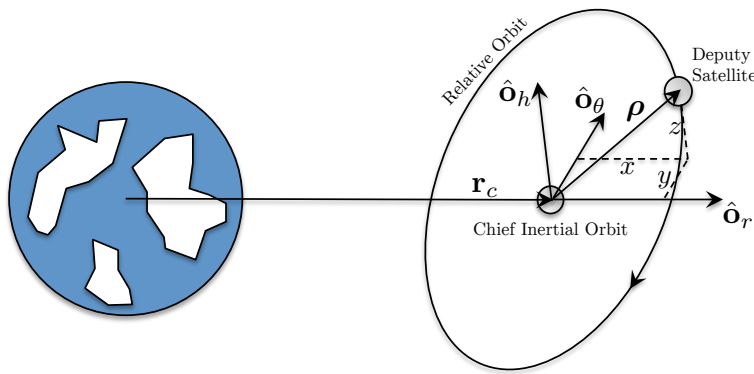


Figure 3: Spacecraft formation flying: Chief with Deputy (Adapted from [4])

The relative orbit of the deputy about the chief is expressed in the Hill frame, also known as the local vertical local horizontal (LVLH) frame, defined by the vector triad  $\{\hat{\mathbf{o}}_r, \hat{\mathbf{o}}_\theta, \hat{\mathbf{o}}_h\}$  using the following expressions,

$$\hat{\mathbf{o}}_r = \frac{\mathbf{r}_c}{r_c}, \quad (9)$$

$$\hat{\mathbf{o}}_\theta = \hat{\mathbf{o}}_h \times \hat{\mathbf{o}}_r, \quad (10)$$

$$\hat{\mathbf{o}}_h = \frac{\mathbf{h}}{h}. \quad (11)$$

Where,  $\mathbf{r}_c$  is the vector from the center of the Earth to the chief satellite and  $\mathbf{h}$  is the angular momentum vector of the chief inertial orbit, see Figure 3 for the diagram. The deputy inertial position vector  $\mathbf{r}_d$  is defined relative to the chief as,

$$\mathbf{r}_d = \mathbf{r}_c + [NO]\rho. \quad (12)$$

Where  $\rho$  is comprised of  $x$ ,  $y$  and  $z$  components in the  $\hat{\mathbf{o}}_r$ ,  $\hat{\mathbf{o}}_\theta$  and  $\hat{\mathbf{o}}_h$  directions respectively and  $[NO]$  is the rotation matrix from the Hill frame  $\mathcal{O}$  to the inertial frame  $\mathcal{N}$ . The  $[NO]$  rotation matrix is defined as,

$$[NO] = [\hat{\mathbf{o}}_r \quad \hat{\mathbf{o}}_\theta \quad \hat{\mathbf{o}}_h]^\top. \quad (13)$$

The deputy inertial velocity vector  $\dot{\mathbf{r}}_d$  is,

$$\dot{\mathbf{r}}_d = \dot{\mathbf{r}}_c + [NO] \left( \frac{\mathcal{O}d\rho}{dt} + \dot{f}\hat{\mathbf{o}}_h \times \rho \right). \quad (14)$$

Where  $\dot{f}$  is the angular velocity of the Hill frame relative to the inertial frame. Because we are assuming 2-body Keplerian motion, the angular momentum of the orbit is constant and the angular velocity can be defined as,

$$\dot{f} = \frac{h}{r_c^2}. \quad (15)$$

The estimated state vector, in the Hill frame is then,

$$\mathbf{X} = [\rho \quad \dot{\rho}] = [x \quad y \quad z \quad \dot{x} \quad \dot{y} \quad \dot{z}]^\top. \quad (16)$$

The time evolution of the states are given by the following dynamics shown in first-order form:

$$\dot{\mathbf{X}}(t) = F(\mathbf{X}, t) = \begin{bmatrix} \dot{x} \\ \dot{y} \\ \dot{z} \\ \ddot{x} \\ \ddot{y} \\ \ddot{z} \end{bmatrix} = \begin{bmatrix} \dot{x} \\ \dot{y} \\ \dot{z} \\ 2\dot{f} \left( \dot{y} - y \frac{\dot{r}_c}{r_c} \right) + x \dot{f}^2 + \frac{\mu}{r_c^2} - \frac{\mu}{r_d^3} (r_c + x) \\ -2\dot{f} \left( \dot{x} - x \frac{\dot{r}_c}{r_c} \right) + y \dot{f}^2 - \frac{\mu}{r_d^3} y \\ -\frac{\mu}{r_d^3} z \end{bmatrix} \quad (17)$$

The dynamics equations shown in Eq. 17 are in exact non-linear form, that allows the deputy satellite to be an arbitrarily large distance away from the chief and the orbits can be eccentric as well while still describing the satellite motion accurately.

The deputy spacecraft is estimated in the Hill frame of the chief, which was up until now simply defined as the  $\mathcal{O}$  frame. But often times rotating the state and uncertainty from the chief LVLH frame to the deputy LVLH frame is more appropriate. In this way the state and uncertainty basis vectors correspond directly with the radial, velocity (for circular orbits only), and angular momentum directions of the deputy spacecraft. To perform this rotation we now discern the Hill or LVLH frame for both the chief and the deputy by using subscripts  $c$  for chief and  $d$  for deputy so that we have the  $\mathcal{O}_c$  and  $\mathcal{O}_d$  frames. The state of the deputy is initially estimated in the chief frame which is represented by  $\mathcal{O}_c \mathbf{X}_d$ , instead we rotate the state into the deputy frame represented by  $\mathcal{O}_d \mathbf{X}_d$  using the LVLH to inertial rotations  $[NO]$  from both the chief and the deputy resulting in the following equation,

$$\mathcal{O}_d \mathbf{X}_d = [NO]_d^\top [NO]_c^{\mathcal{O}_c} \mathbf{X}_d. \quad (18)$$

Similarly, the covariance of the deputy is initially estimated in the chief frame represented by  $\mathcal{O}_c \mathbf{P}_d$ , and is rotated into the deputy frame represented by  $\mathcal{O}_d \mathbf{P}_d$  resulting in the following equation,

$$\mathcal{O}_d \mathbf{P}_d = [NO]_d^\top [NO]_c^{\mathcal{O}_c} \mathbf{P}_d [NO]_c^\top [NO]_d. \quad (19)$$

All plots in this paper show the state and uncertainty in the  $\mathcal{O}_d \mathbf{X}_d$  and  $\mathcal{O}_d \mathbf{P}_d$  frame respectively unless specified otherwise.

In the following section we examine the effectiveness of using TDOA and FDOA by analyzing the Cramér-Rao Lower Bound (CRLB) of the chief and deputy pair at semi-major axes ranging from LEO to GEO. In the following scenarios three stations are used in addition to the reference station to create three baselines. Table 1 lists the exact locations used in these simulations. Notice that the locations of the RXs are also listed but do not actually influence the solution in anyway because the frequencies used by the TXs are all the same (14.3 GHz), consequently, the downlink legs cancel in the FDOA measurement equation as well.

The apriori uncertainties needed for computing the CRLB are listed in Table 2. Both the TDOA/FDOA and range/range-rate uncertainties are included, the latter of which is used later on for CRLB comparison with the TDOA/FDOA results.

Table 2: CRLB  $1\sigma$  a-priori uncertainty for estimated states and measurements

<i>Satellite state uncertainty</i>	
Position	10 km
Velocity	10 m/s
<i>Measurement uncertainty</i>	
TDOA	0.035 $\mu$ s
FDOA	0.2 mHz
Range	1 m
Range-Rate	1 mm/s

## 4 Orbit Determination of Bounded Relative Motion Case

We examine a formation flying setup in very close proximity to each other showing that regardless of the very small separation between the two spacecraft, the TDOA and FDOA measurements are well-suited for OD in this situation. The chief satellite orbit is listed in Table 3 and the Deputy satellite orbit is described next.

Table 3: Orbital Elements for Chief Orbit Ranging from LEO to GEO

	a [km]	e	i [deg]	$\Omega$ [deg]	$\omega$ [deg]	v [deg]
Chief	6746.26 - 48910.40	0	0	0	0	255

### 4.1 Deputy Equations of Motion for Bounded Relative Motion

To compute a bounded relative motion trajectory of the deputy about the chief we use the following set of equations:

$$\begin{aligned}
 \mathcal{O}_c x_d &= A_0 \cos(\mathcal{O}_c \dot{f} t + \alpha) \\
 \mathcal{O}_c y_d &= -2A_0 \sin(\mathcal{O}_c \dot{f} t + \alpha) + y_{offset} \\
 \mathcal{O}_c z_d &= B_0 \cos(\mathcal{O}_c \dot{f} t + \beta) \\
 \mathcal{O}_c \dot{x}_d &= -A_0 (\mathcal{O}_c \dot{f}) \sin(\mathcal{O}_c \dot{f} t + \alpha) \\
 \mathcal{O}_c \dot{y}_d &= -2A_0 (\mathcal{O}_c \dot{f}) \cos(\mathcal{O}_c \dot{f} t + \alpha) \\
 \mathcal{O}_c \dot{z}_d &= -B_0 (\mathcal{O}_c \dot{f}) \sin(\mathcal{O}_c \dot{f} t + \beta)
 \end{aligned} \tag{20}$$

Where  $A_0$  and  $B_0$  are the cyclic amplitudes of the relative orbit in-plane and out-of-plane components respectively. The phase angles of the cyclic motion are defined by  $\alpha$  and  $\beta$  for the in-plane and out-of-plane components correspondingly, and the along-track offset is defined by  $y_{offset}$ . The true anomaly rate of the chief is represented by  $\dot{f}$  and is previously defined by Eq. 15.

Table 4 lists two cases with a  $\pi/2$  in-plane phase difference. As a consequence we obtain the two relative orbit plots shown in Figure 4.

Table 4: Relative orbit Parameters for Face-On and Edge-On relative orbits

Case	$A_0$ [km]	$B_0$ [km]	$t$ [s]	$\alpha$ [rad]	$\beta$ [rad]	$y_{offset}$ [km]
1	1	2	0	0	0	0
2	1	2	0	$\pi/2$	0	0

Both cases were examined, but whether the relative orbit was face-on or edge-on had no impact on the OD accuracy. Therefore we only show the OD results using the face-on (case 1) relative orbit.

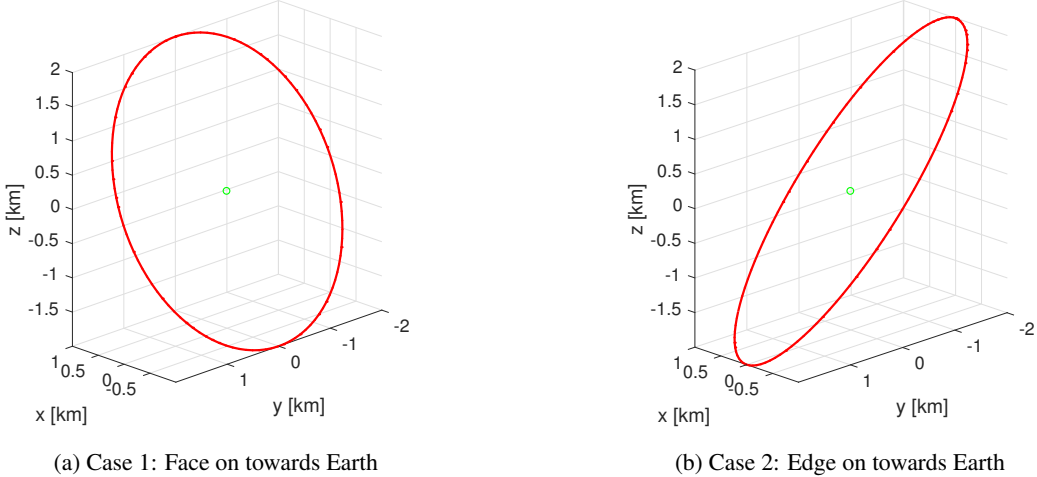


Figure 4: Relative orbits of cases in Table 4. Green central circle is the Chief, red line is relative deputy orbit. Plotted in the chief Hill frame.

## 4.2 Estimating the Deputy with Perfect Chief Knowledge

We first show, in Figure 5, the CRLBs of varying chief orbits with a tightly orbiting deputy spacecraft, assuming perfect state knowledge on the chief. The abscissa has the time of the observation span with an observation interval of 3 minutes, the ordinate varies the chief semi-major axis, and the color denotes the magnitude of the covariance. Six plots are shown, each corresponding to one of the states of the deputy satellite in the LVLH frame. We find that the state uncertainty of the deputy is primarily dominated by the inertial geometry of the deputy with respect to the stations rather than with respect to the chief satellite as long as the state knowledge of the chief is known perfectly. As the chief and deputy satellite formation increases in semi-major axis, thereby reducing the relative velocity with respect to the stations, the amount of information content present is lower, therefore the covariance does not drop as much as with a smaller semi-major axis. Note that in the  $\hat{\mathbf{o}}_{d\theta}$  direction, the deputy in-track position, shown in Figure 5(c), there is a region of reduced observability when the chief satellite is in a GEO orbit. The covariance remains nearly at its original uncertainty over the entire time data is gathered due to the non-existent relative velocity of the deputy with respect to the stations. In all other scenarios however, the covariance drops quickly and to very low levels of uncertainty as shown by the ubiquity of the light blue color.

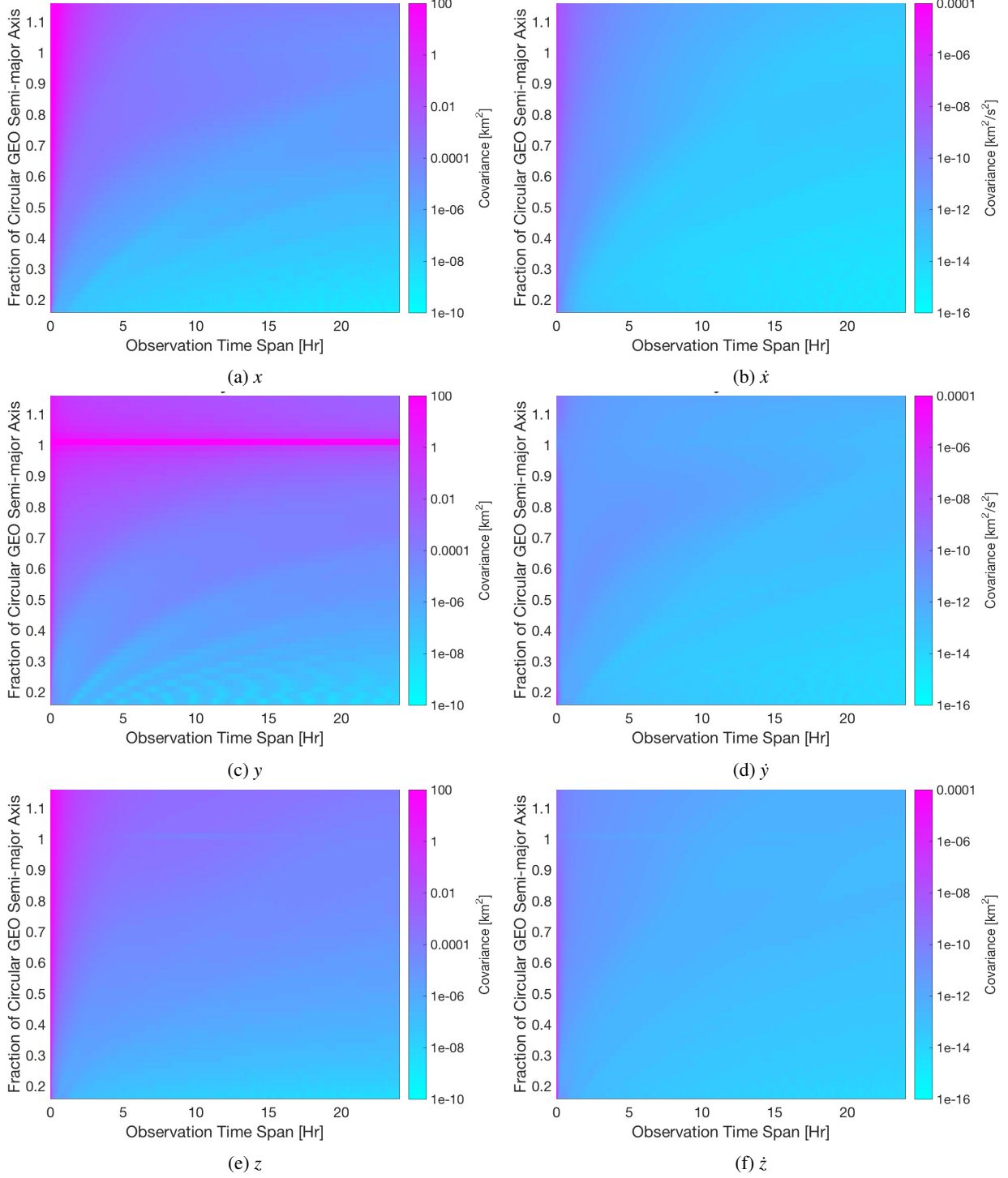
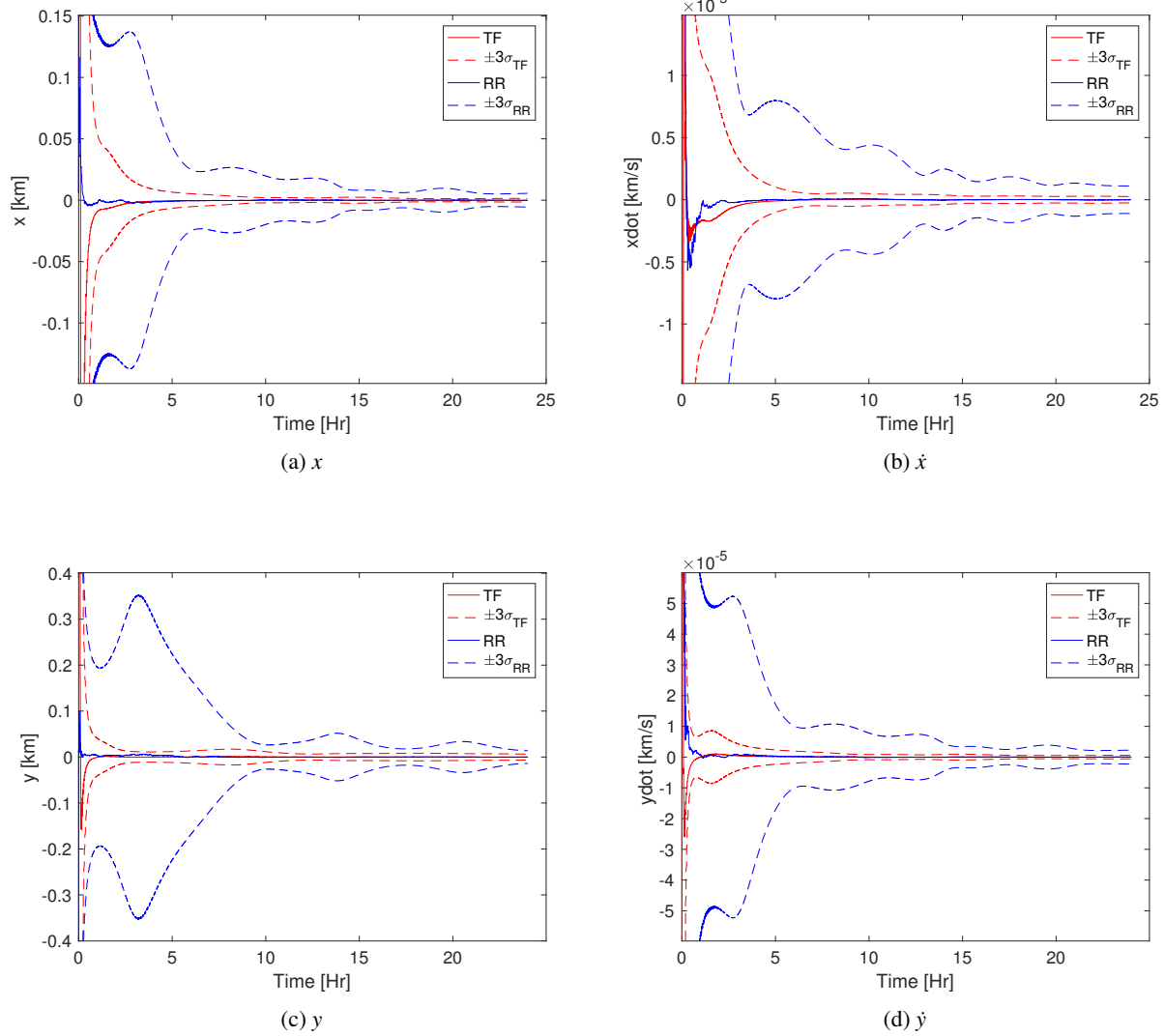


Figure 5: Close proximity bounded relative motion at various semi-major axes, shown on ordinate. Showing CRLB covariance over various observation time spans shown on abscissa. Coordinates are in the LVLH frame of the deputy. Three stations plus reference station are used.

In Figure 6 we compare the OD results using TDOA/FDOA and range/range-rate in each case with the formation flight in a MEO orbit with a semi-major axis of  $0.5 \times a_{GEO}$ . The solid red line is the TDOA/FDOA state error while the dashed red line is the TDOA/FDOA  $\pm 3\sigma$  covariance bounds. Range and range-rate are shown in a similar manner with

blue. The state errors in both cases are comparable and driven to zero from the initial state perturbation from the truth of 10 km in each direction for position and 10 m/s in each direction for velocity. The TDOA and FDOA observables constrain the uncertainty much faster and to a lower degree however, making them more favorable. Furthermore, recall that one of the key benefits of using TDOA and FDOA is the cancellation of common errors, therefore if a clock bias exists, the TDOA and FDOA state error would be as shown, but unless estimated with the range and range-rate system, those results would be significantly biased and likely even exceed its  $\pm 3\sigma$  covariance bounds.



We expand the comparison beyond the MEO case shown in Figure 6 to include semi-major axes of the formation flight pair from LEO to GEO, this is shown in Figure 7. This plot is similar to Figure 5, the abscissa and ordinate are the same, but rather than showing the absolute covariance values we now show the percent difference between the TDOA/FDOA and range/range-rate covariances. Yellow means a lower covariance value using TDOA and FDOA while blue indicates that the covariance is lower using range and range-rate. There is only one large region, in the in-track direction, shown on Figure 7(c) that performs poorly using TDOA and FDOA. It corresponds to the low observability region of a GEO chief shown in Figure 5(c). Notice the strength of the TDOA/FDOA observables in the cross-track direction, shown in Figures 7(e) and 7(f).

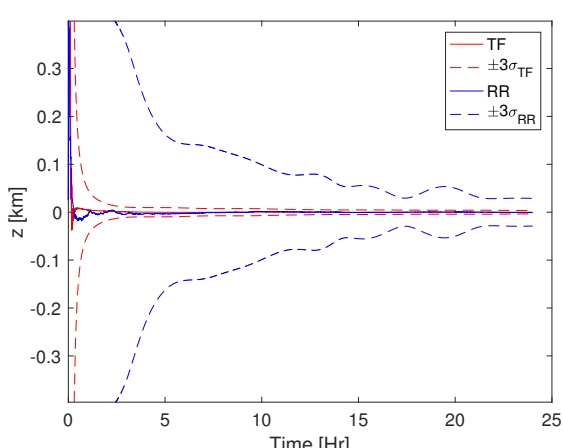
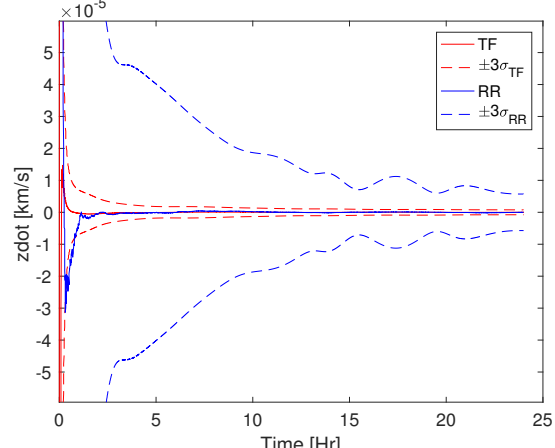
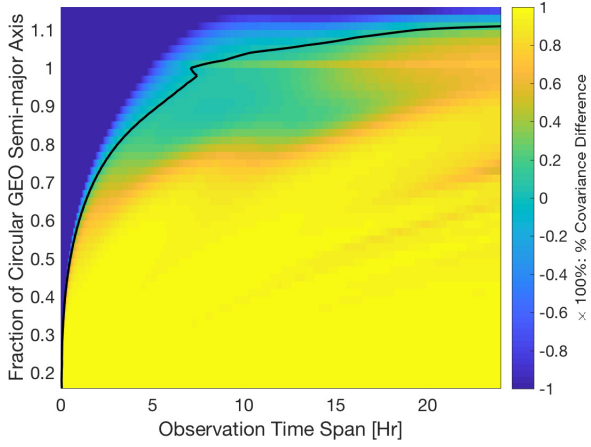
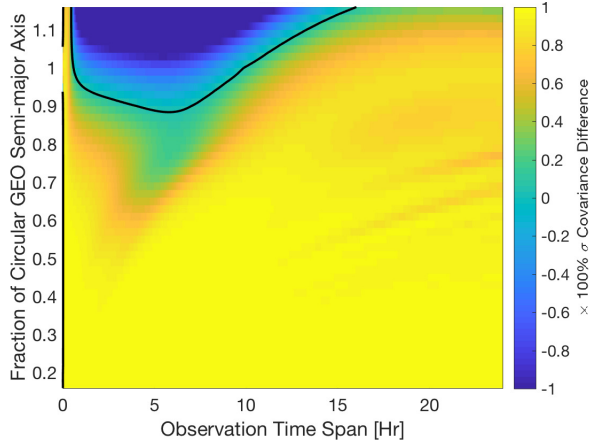
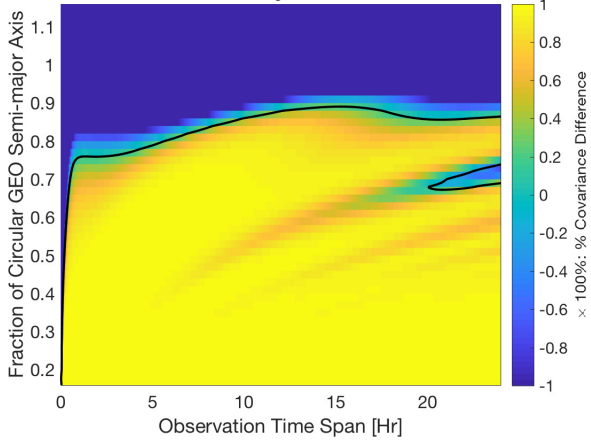
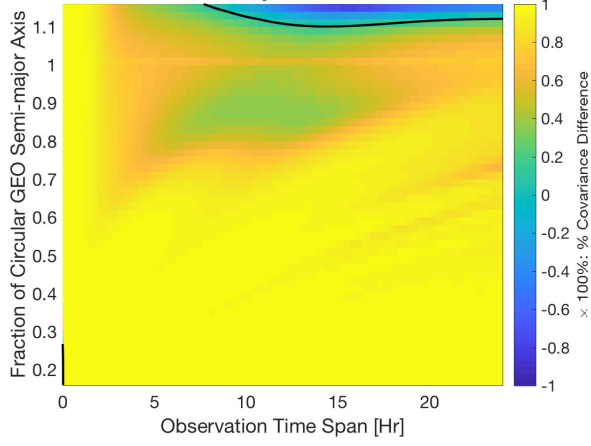
(e)  $z$ (f)  $\dot{z}$ 

Figure 6: State error and  $3\sigma$  covariances for close proximity bounded relative motion with chief at MEO ( $0.5 \times a_{GEO}$ ) in the deputy LVLH frame. Comparison between TDOA/FDOA (TF) and Range/Range-Rate (RR) observables. Three stations plus reference station are used.

(a)  $x$ (b)  $\dot{x}$ (c)  $y$ (d)  $\dot{y}$

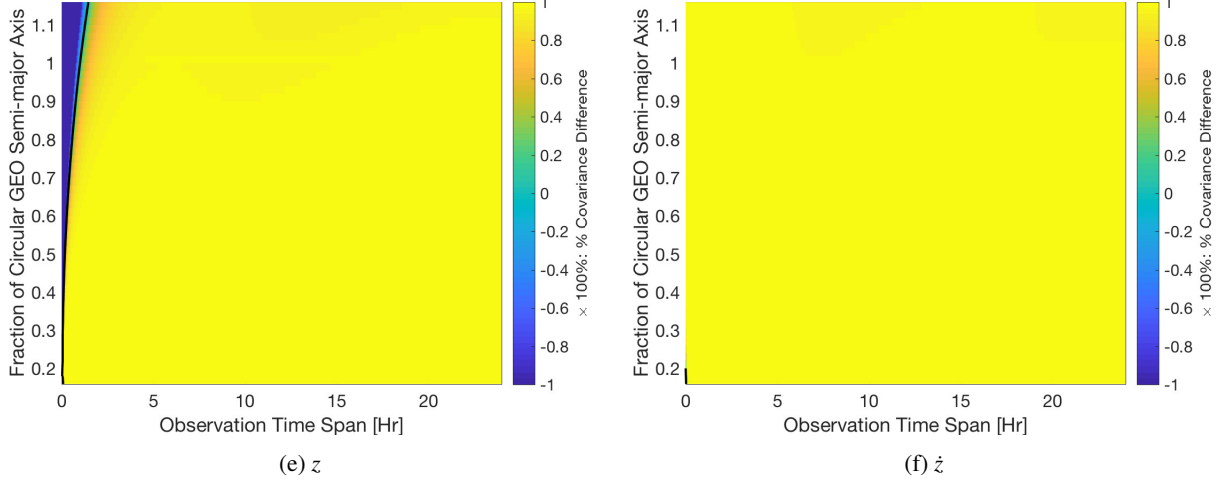


Figure 7: Close proximity bounded relative motion at various semi-major axes, shown on ordinate. Showing % difference of CRLB covariance bounds between TDOA/FDOA and Range/Range-Rate measurements over various observation time spans shown on abscissa. Color values above 0 indicate a region where TDOA/FDOA has lower covariance bounds compared to Range/Range-Rate and vice versa. Coordinates are in the LVLH frame of the deputy. Three stations plus reference station are used.

### 4.3 Estimating the Deputy with Considered Chief Uncertainty

To increase the realism of the relative OD case of a close proximity satellite formation we now look at the instance where a chief position uncertainty of 10 m in each direction and velocity uncertainty of 1 mm/s in each direction is considered. The chief uncertainty effect upon the CRLBs does not change the results significantly from those found without the included uncertainty in Figure 7. The same features are encountered, with the low observability of the in-track position at GEO occurring once more.

We scrutinize the GEO case more closely and run a simulation case to see how the low observability in  $y$  affects the filter solution. The SR-USKF is initiated with an a-priori state off from the truth by 10 km in position in each direction and 10 m/s in velocity in each direction as well. Figure 9(a) shows the chief satellite in green at the origin with the deputy truth orbit shown in red. The estimated deputy orbit is shown in blue which started from the a-priori state and moved its way over to the truth trajectory in all components except for  $y$  as predicted by the CRLB. The residuals are shown in Figure 9(b). The TDOA residuals clearly indicate that the estimated solution is not perfect, while the FDOA residuals are fitted to the noise. A sequential filter like the SR-USKF is not generally iterated but by iterating it anyway the solution can slowly be walked over closer to the truth trajectory as indicated by the estimated trajectory and residuals shown in Figures 9(c) and (d) respectively. The ability to obtain a better solution after many iterations suggests that the issue is numerical and a better method to obtain the best estimate likely exists. One such a method may be to compute multiple a-priori states after the first iteration, which vary in the in-track direction, in effect using a line-search rather than waiting for the filter to slowly converge upon a solution with residuals in the noise.

We can show that the low observability in  $y$  only occurs at GEO by doing the same test using a satellite formation pair positioned at  $0.95 \times a_{GEO}$ . Figure 10 exhibits no symptoms of numerical problems, and instead quickly snaps to the correct solution. The estimated solution, shown in blue, is coincident to the truth trajectory and the residuals are fitted to the noise.

As previously shown with perfect chief knowledge, we also compare TDOA/FDOA with range/range-rate for bounded formation flying with chief satellite uncertainty considered when the satellite pair is at MEO ( $0.5 \times a_{GEO}$ ). Once again, the TDOA/FDOA  $3\sigma$  covariance bounds are much smaller than those of range and range-rate while the state errors tend to be comparable, illustrated in Figure 11.

Finally, we expand beyond just the MEO case and plot orbits ranging from LEO to GEO and compare the TDOA/FDOA CRLBs with range/range-rate shown in Figure 12. Significant portions of each of the position and velocity components have lower CRLBs using the TDOA and FDOA observables.

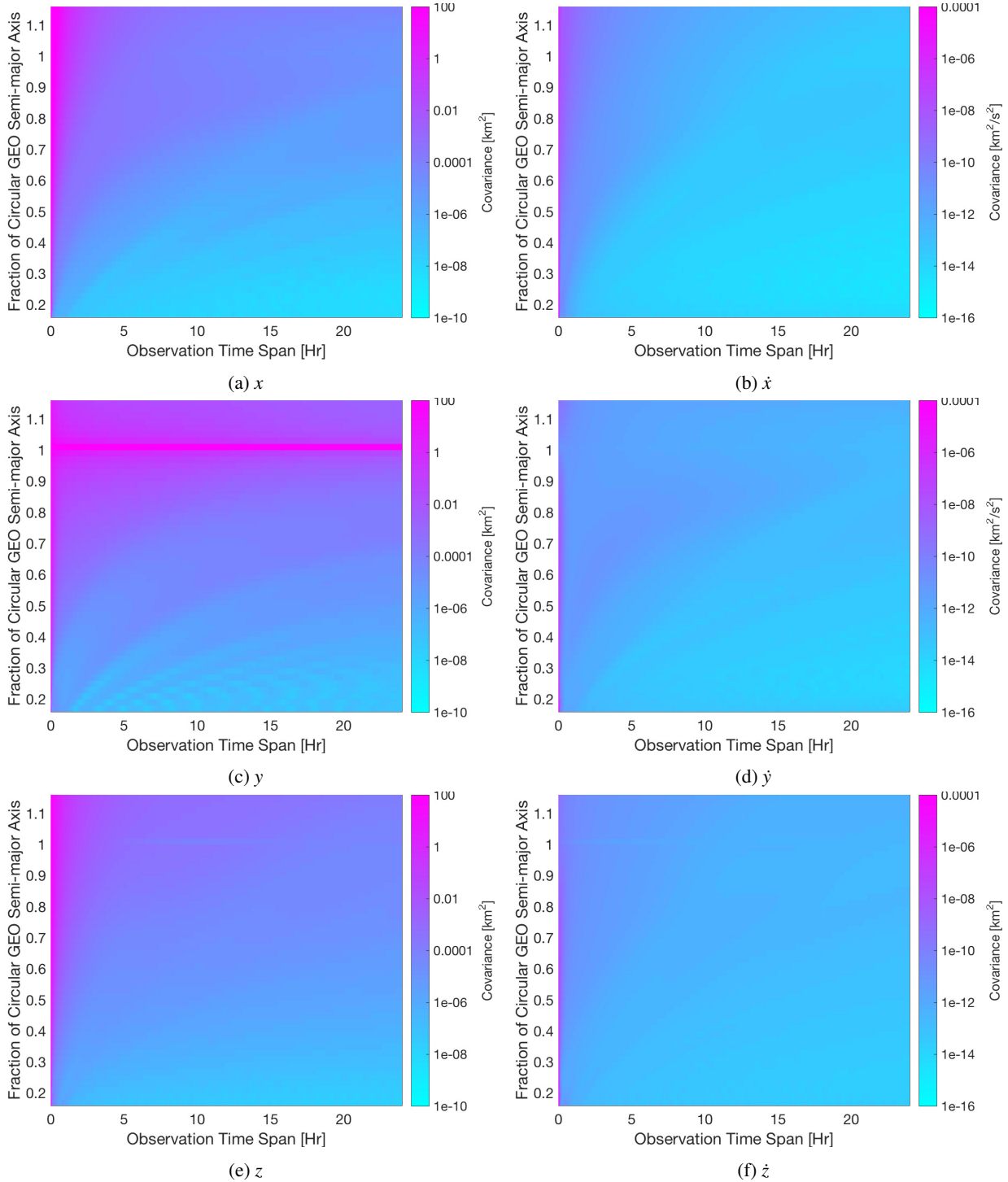
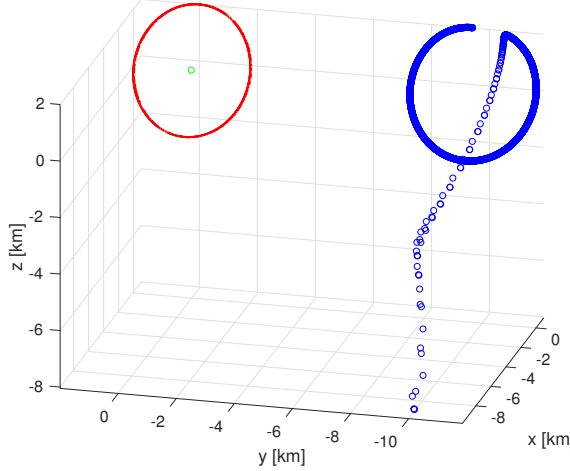
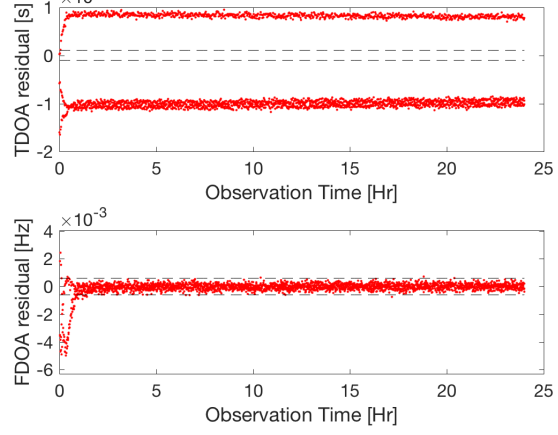


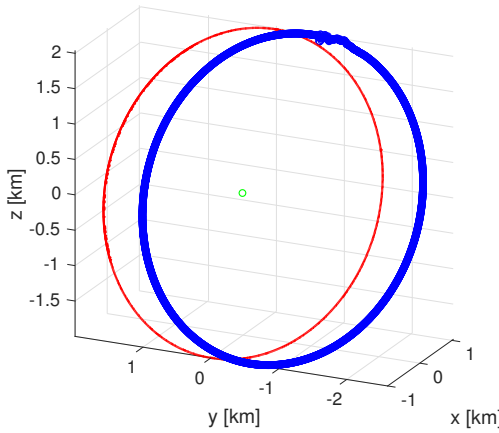
Figure 8: Close proximity bounded relative motion with considered  $1\sigma$  position uncertainty of 10 m and  $1\sigma$  velocity uncertainty of 1 mm/s in each direction of the chief at various semi-major axes, shown on ordinate. Showing CRLB covariance over various observation time spans shown on abscissa. Coordinates are in the LVLH frame of the deputy. Three stations plus reference station are used.



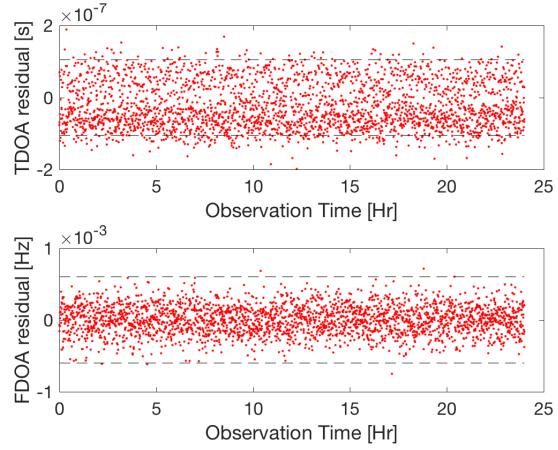
(a) Estimated vs truth state after 1 iteration of SR-USKF



(b) TDOA and FDOA residuals after 1 iteration of SR-USKF

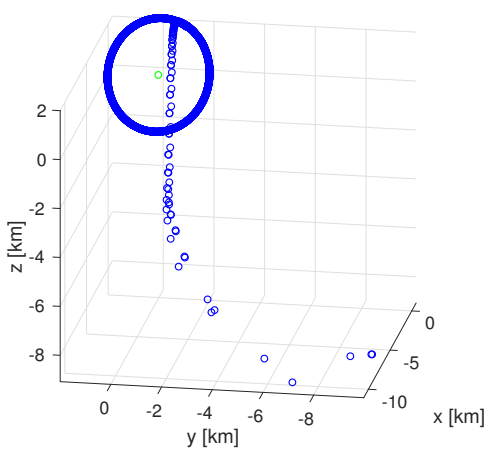


(c) Estimated vs truth state after 92 iterations of SR-USKF

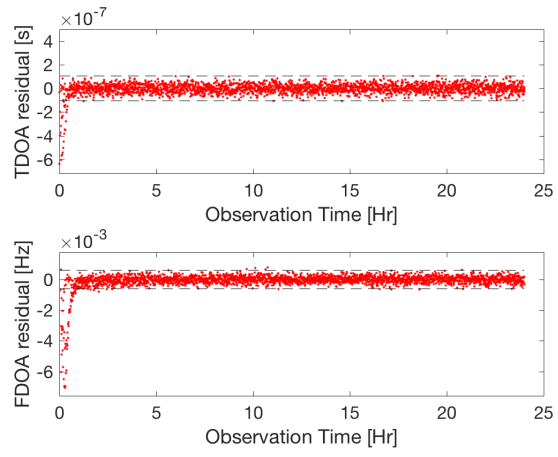


(d) TDOA and FDOA residuals after 92 iteration of SR-USKF

Figure 9: Close proximity bounded relative motion with considered  $1\sigma$  position uncertainty of 10 m and  $1\sigma$  velocity uncertainty of 1 mm/s in each direction of the chief. Satellite formation pair in GEO orbit resulting in low observability in the in-track y position direction of deputy. Comparing 1<sup>st</sup> to 92<sup>nd</sup> iteration.

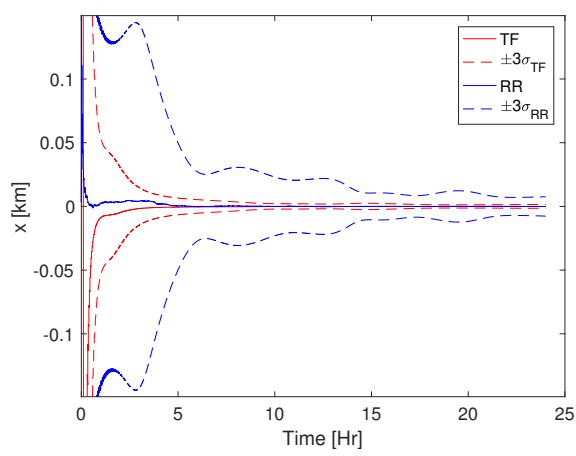


(a) Estimated vs truth state after 1 iteration of SR-USKF

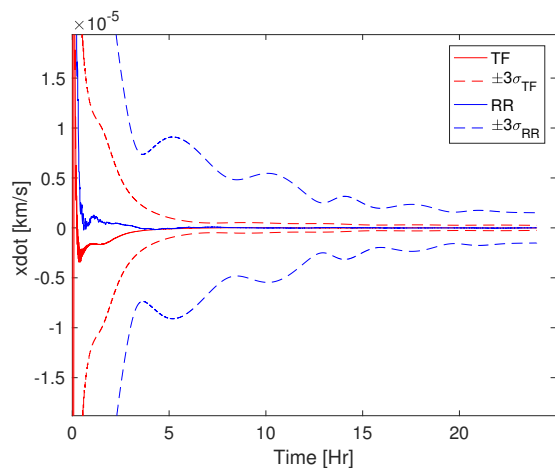


(b) TDOA and FDOA residuals after 1 iteration of SR-USKF

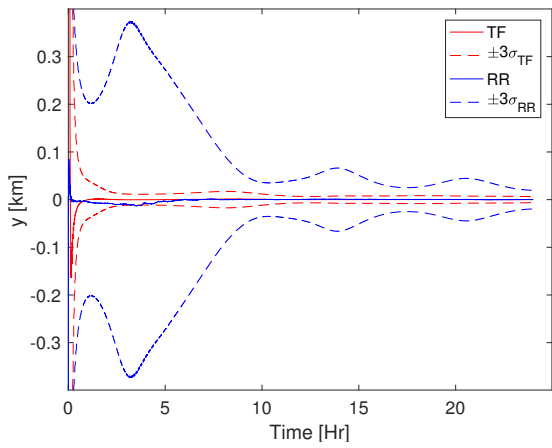
Figure 10: Close proximity bounded relative motion with considered  $1\sigma$  position uncertainty of 10 m and  $1\sigma$  velocity uncertainty of 1 mm/s in each direction of the chief. Chief in  $0.95 \times a_{GEO}$  orbit demonstrating the low observability in the in-track y position direction is limited to GEO only and not its neighboring orbits.



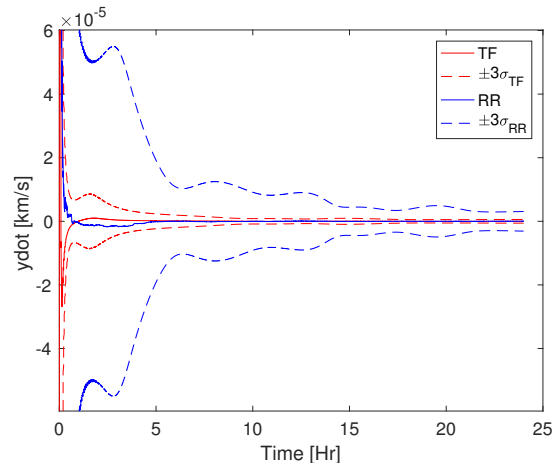
(a)  $x$



(b)  $\dot{x}$



(c)  $y$



(d)  $\dot{y}$

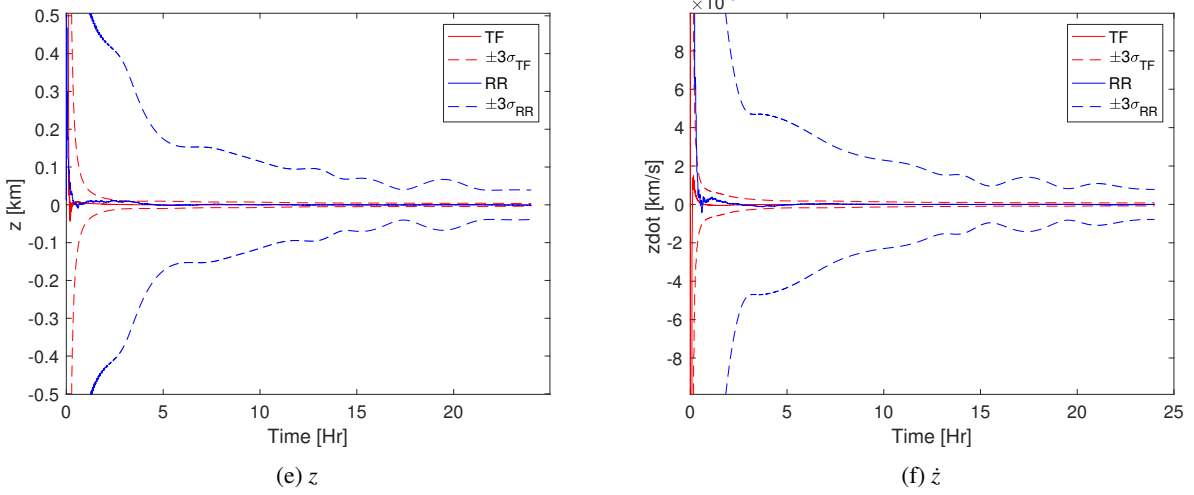
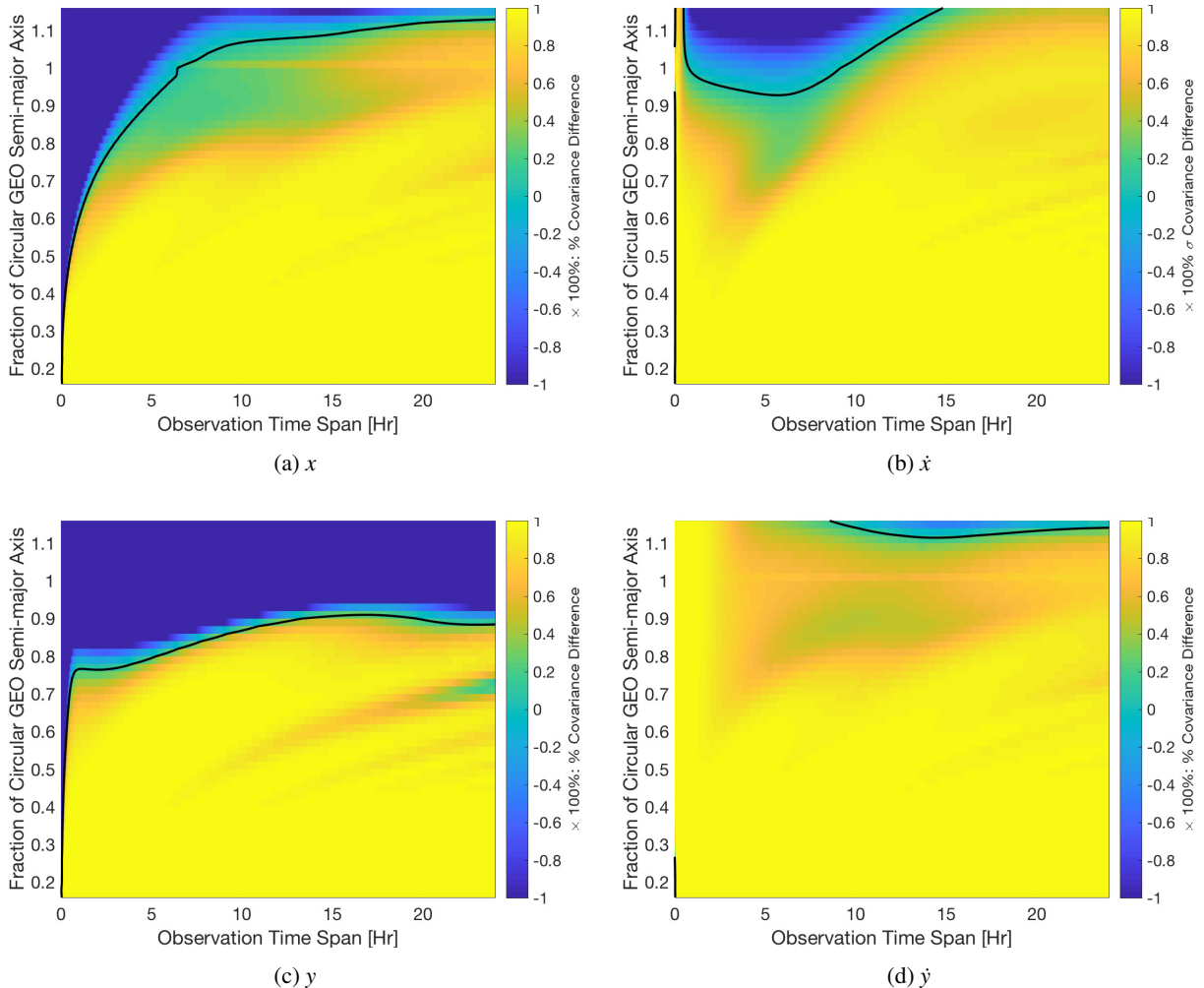


Figure 11: State error and  $3\sigma$  covariances for close proximity bounded relative motion with considered  $1\sigma$  position uncertainty of 10 m and  $1\sigma$  velocity uncertainty of 1 mm/s in each direction of chief with chief at MEO ( $0.5 \times a_{GEO}$ ) in the deputy LVLH frame. Comparison between TDOA/FDOA (TF) and Range/Range-Rate (RR) observables. Three stations plus reference station are used.



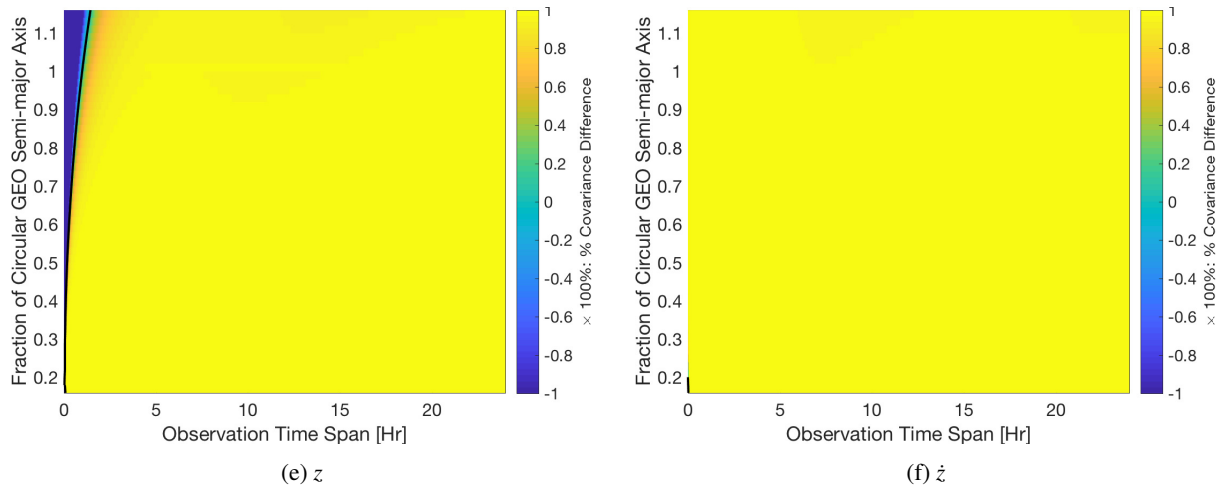
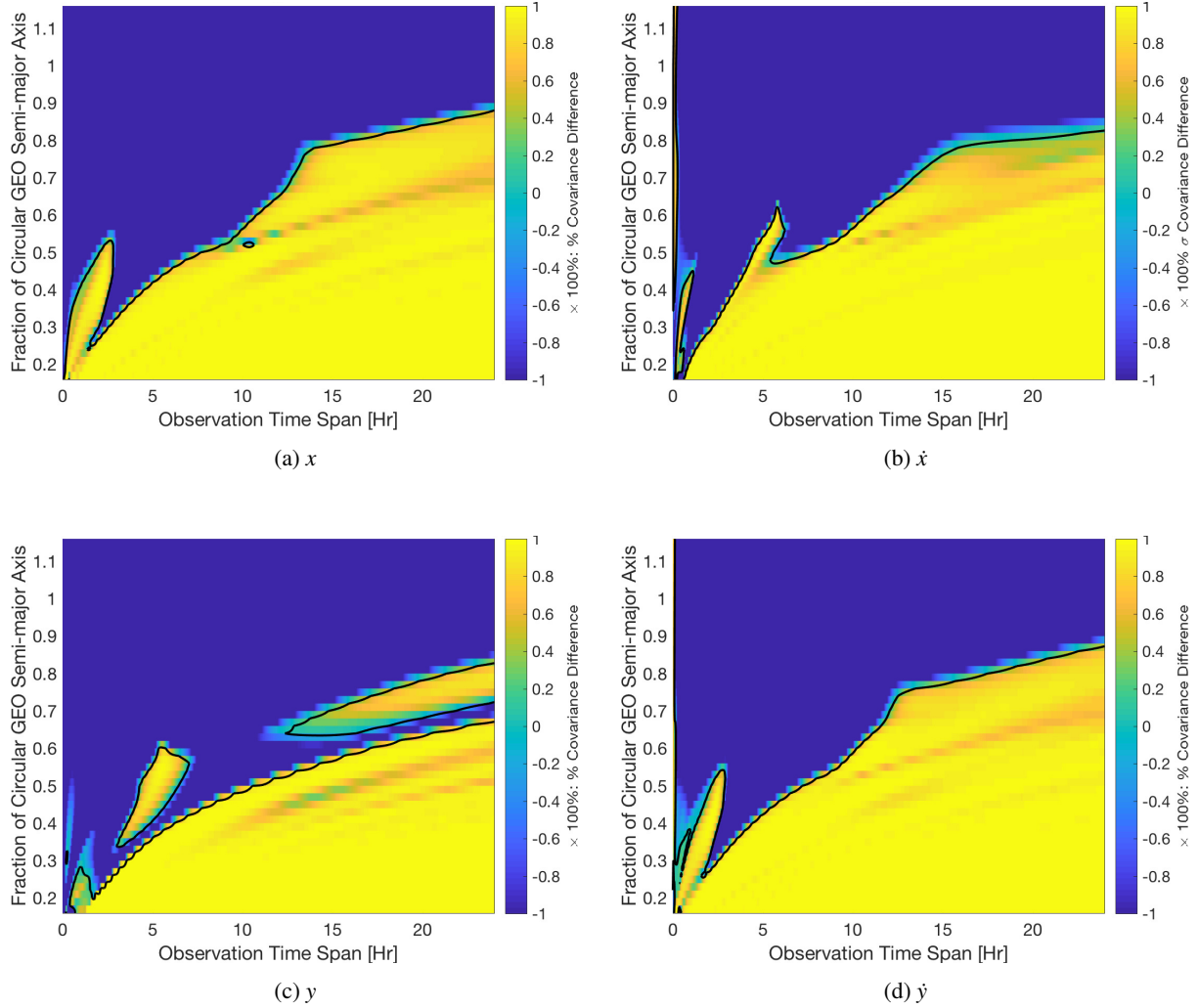


Figure 12: Close proximity bounded relative motion with considered  $1\sigma$  position uncertainty of 10 m and  $1\sigma$  velocity uncertainty of 1 mm/s in each direction of the chief at various semi-major axes, shown on ordinate. Showing % difference of CRLB covariance bounds between TDOA/FDOA and Range/Range-Rate measurements over various observation time spans shown on abscissa. Color values above 0 indicate a region where TDOA/FDOA has lower covariance bounds compared to Range/Range-Rate and vice versa. Coordinates are in the LVLH frame of the deputy. Three stations plus reference station are used.

### 4.3.1 Estimating the Deputy with Considered Chief Uncertainty and One Baseline

In the previous cases in this paper we have shown the results using three baselines employing the stations listed in Table 1. In this final scenario we take the previous bounded relative motion case and only use one station, to create one baseline, the Boulder-San Diego baseline. The results are presented in Figure 13. In this scenario there are distinct orbital regimes that would benefit from the TDOA/FDOA and the range/range-rate measurement set. More specifically, when faster dynamics, as is the case with lower orbiting satellites, are present along with longer observation times TDOA and FDOA are preferred. In the higher orbits with shorter observation spans range and range-rate has a lower CRLB.



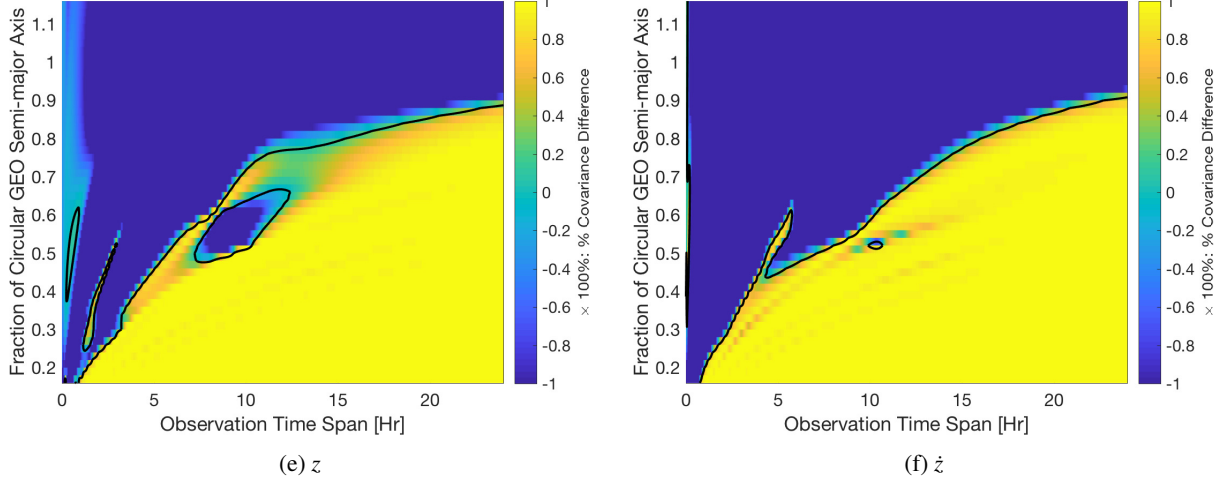


Figure 13: Close proximity bounded relative motion with considered  $1\sigma$  position uncertainty of 10 m and  $1\sigma$  velocity uncertainty of 1 mm/s in each direction of the chief at various semi-major axes, shown on ordinate. Showing % difference of CRLB covariance bounds between TDOA/FDOA and Range/Range-Rate measurements over various observation time spans shown on abscissa. Color values above 0 indicate a region where TDOA/FDOA has lower covariance bounds compared to Range/Range-Rate and vice versa. Coordinates are in the LVLH frame of the deputy. One station plus reference station is used.

## 5 Conclusion

When multiple TXs are available, and therefore multiple baselines can be established, OD using TDOA and FDOA can provide significant improvements in the solution uncertainty. This is especially true when the range and range-rate measurements also have un-estimated biases present, which are automatically canceled using TDOA and FDOA and therefore do not impact the solution. When only one baseline is used there are large regions which benefit from range and range-rate OD and large regions where TDOA and FDOA are better. The faster the satellites move with respect to the tracking stations the more likely that TDOA and FDOA will be favorable to using range and range-rate. Furthermore the TDOA and FDOA observables are especially strong in the cross-track direction for both position and velocity and can reduce that uncertainty very quickly. With the reduced state uncertainty, operators can make more informed decisions regarding collision probabilities and the need to or not to maneuver a spacecraft.

## References

- [1] M H Chan. Application of a Dual Satellite Geolocation System on Locating Sweeping Interference. In *World Academy of Science, Engineering and Technology*, volume 6, pages 939–944, 2012.
- [2] Jeroen L. Geeraert and Jay W. McMahon. Square-Root Unscented Schmidt-Kalman Filter. *Journal of Guidance, Control, and Dynamics*, 2017.
- [3] K. C. Ho and Y. T. Chan. Solution and Performance Analysis of Geolocation by TDOA. *IEEE Transactions on Aerospace and Electronic Systems*, 29(4):1311–1322, 1993.
- [4] Hanspeter Schaub and John L. Junkins. *Analytical Mechanics of Space Systems*. American Institute of Aeronautics and Astronautics, second edition, 2009.
- [5] Seymour Stein. Algorithms for Ambiguity Function Processing. *IEEE Transactions on Acoustics, Speech, and Signal Processing*, 29(3):588–599, 1981.